Journal of Sustainable Construction Materials and Technologies

Volume 11 | Issue 2 Article 6

Modeling of Tensile Stress-Strain Response for Steel Fiber Reinforced Self-Compacting Concretes

Anıl Niş

Department of Civil Engineering, Istanbul Gelisim University, Istanbul, Türkiye, anis@gelisim.edu.tr

Nilufer Özyurt

Department of Civil Engineering, Boğaziçi University, Istanbul, Türkiye

Turan Özturan

Department of Civil Engineering, Boğaziçi University, Istanbul, Türkiye

Recommended Citation

Niş, Anıl; Özyurt, Nilufer; and Özturan, Turan (2026) "Modeling of Tensile Stress-Strain Response for Steel Fiber Reinforced Self-Compacting Concretes," *Journal of Sustainable Construction Materials and Technologies*: Vol. 11: Iss. 2, Article 6.

https://doi.org/10.29187/2458-973X.1222

Available at: https://commons.yildiz.edu.tr/jscmt/vol11/iss2/6

JOURNAL OF SUSTAINABLE CONSTRUCTION MATERIALS AND TECHNOLOGIES 2026;11:289–304

RESEARCH ARTICLE

Modeling of Tensile Stress-Strain Response for Steel Fiber Reinforced Self-Compacting Concretes

Anıl Niş [a,*], Nilufer Özyurt [b], Turan Özturan [b]

[a] Department of Civil Engineering, Istanbul Gelisim University, Istanbul, Türkiye
[b] Department of Civil Engineering, Boğaziçi University, Istanbul, Türkiye

ABSTRACT

Main aim of the research was to further understand self-compacting concrete reinforced with steel fibers (SFR-SCC) behavior and to contribute modeling of the tensile stress-strain diagrams for the standardization of the fiber reinforced materials for structural utilization. Fiber reinforced materials has not been used without structural rebar because of the absence of stress-strain curve in tension required for the structural design codes. Hence, an inverse analysis (multi-layer model) was further modified for various steel fibers to predict tensile stress-strain behaviour. For this purpose, 5 different mixes; control, reinforced with long fibers with 0.5% and 1%, short fiber with 0.5% and hybrid fiber with 1% fiber volume were produced. Fresh state tests were realized to examine flow capability of the mixes. For the input parameters, force and displacement controlled compressive strength tests and splitting tensile strength tests were realized on the SFR-SCC specimens. Three-point flexural strength tests on notched beams were realized to check experimental results with the model simulation results. The results showed that previous models were applicable for long fibrous specimens; however, further improvements were required for long FRC specimens. For the short and hybrid FRC samples, novel parameters were successfully proposed and utilized in this study.

Keywords: Multi layer model, Fiber reinforced materials, SCC, Hybrid fibers, Flexural modeling

1. Introduction

The self-compacting concrete reinforced with steel fibers (SFR-SCC) takes great attention in structural applications due to the enhanced mechanical and durability performance. The self-compacting concrete (SCC) is a homogeneous flowable material, which eliminates bleeding, segregation, and compaction problems emerged in conventional concretes by means of its compaction under its self-weight [1]. The straight short steel fibers are incorporated into the matrix to achieve superior mechanical strength [2], whilst the long hooked-end steel fibers are introduced to decrease the cost and improve the deformation capacity of a concrete [3]. Also, a combination of both hooked-end long and straight short fibers (hybrid fibers) is utilized to reduce the cost and obtain the moderate mechanical performance [4]. By integrating two various materials, SFR-SCC achieves enhanced flexibility, improved durability, and higher strength compared to conventional cement-based materials.

The steel fiber (SF) addition does not generally influence compressive strength and elastic modulus, while the post-peak performance, toughness, and strain capacity of concrete were significantly improved by the inclusion of steel fiber [5, 6]. Also, the existence of steel fibers reduces the crack spacing and widths, therefore both crack control and more ductile concrete behavior were achieved by the inclusion of steel fibers [7, 8]. The favorable contribution of the steel fibers relies on its type, geometry, volume, length, aspect ratio, and the orientation of the steel fibers [9–12]. Amongst the influencing parameters,

Received 11 February 2026; revised 3 June 2026; accepted 7 June 2026.
Available online 16 June 2026

* Corresponding author.
E-mail address: anis@gelisim.edu.tr (A. Niş).

https://doi.org/10.29187/2458-973X.1222

the most significant parameter can be considered as the steel fiber volume content. The steel fiber volume can be classified as low (≤1%), moderate (>1% and <2%), and high (>2%) fiber volume fractions [13], and 1 % steel fiber volume considered to be low steel fiber fraction [14–16]. For the adequate passing ability properties of SCC and costs, the optimum steel fiber volume is considered to be 1% for the structural applications [17, 18].

The effects of different fiber reinforcements on the mechanical strength improvements in the cementitious systems were investigated thoroughly [19–23]. With further research, SFR-SCC is expected to be increasingly adopted in the design stage, particularly in applications where steel fibres can fully replace conventional steel reinforcement [24]. However, the lack of detailed and comprehensive international building standards and the lack of confidence on the essential principles is the main reason behind the underutilization as a structural material [25]. For the standardization process, the fracture parameters, especially post-cracking responses of the material are required for the structural analysis. For this aim, stress versus crack opening relationship (σ-w) is the most appropriate constitutive model for the characterization of these composites when modeling the behavior of a concrete with low (≤1%) steel fiber amounts [26].

The uniaxial tensile test is the best option for the determination of post-cracking response of the steel fibrous concrete; however, there is no uniaxial standard test method is available and different uniaxial test configurations (dog bone, cylinder with various sizes), and various test procedures (set-up and gripping system) are required to obtain post-peak response of the SFRC [25]. For this reason, ongoing studies have been carried out to obtain stress versus crack width relationship (σ-w) indirectly by inverse analysis method using simple test configurations. Amongst the indirect test methods, three-point or four-point bending test methods on the prismatic specimens are preferred due to the easy application compared to a direct tensile test [5, 27]. Therefore, the tensile behaviour can be determined through inverse analysis of the bending test results, based on the stress–crack width (σ–w) relationship for the utilization of SFRC in structural applications [28].

There are various methods available in the literature to model tensile behavior of fibrous concrete: a) Stress versus strain relationships and stress versus crack with relationships, b) Inverse model and direct model, c) Macro and micro scale research levels, and d) continuously differentiable and non-differentiable diagrams. However, fundamental aspects of these methods are still required to be further developed to obtain in-depth and comprehensive knowledge for the future international codes/standards [25]. In this study, a multilayer model (inverse model) is selected to model stress-crack width relationship (σ-w) of the SFRC; therefore, the knowledge regarding the progress of the multilayer model is explained herein.

In the literature, multilayer models for the tensile stress versus crack width (σ-w) relationships or strain softening behavior based on the inverse analysis [29–32] of the experimental test results were proposed. First, an equilibrium based multilayer beam model was developed by Hordijk [29]. Then, Kooiman [30] showed that the multilayer model is also appropriate for the modeling of the fiber reinforced concrete (FRC) specimens. Later, Grünewald [31] proposed a model for self-compacting FRC, which was subsequently modified by Lappa [32] to account for ultra-high-strength FRC specimens. Nevertheless, the results indicated that the existing predictive models fail to accurately capture the tensile response of a broad range of fiber-reinforced concrete types, which has limited the integration of such materials into structural design practices. Thus, supplementary adjustment of the available multilayer models is required for the standardization process of the fibrous materials. In this study, an equilibrium-based multilayer model is employed and further extended to represent the behaviour of long SFRC materials, and new input/design parameters were proposed to the literature for the short and hybrid SFRC materials. The study demonstrated that fiber geometry and distribution substantially influence crack bridging capacity, characteristic crack width, energy dissipation, and load transfer mechanisms. Particularly, the successful establishment of novel tensile input parameters for short and hybrid fiber-reinforced mixtures fills an important gap in the literature, since such systems often exhibit more complex fracture mechanisms than conventional long-fiber SFRC. In addition, by improving the accuracy of tensile constitutive modeling, the study supports the safer and more efficient design of SFRC structural elements subjected to cracking and fracture-dominated loading conditions. Therefore, the research not only advances the current scientific understanding of SFRC behavior but also offers practical modeling guidance for finite element simulations, performance-based design approaches, and future development of fiber-reinforced cementitious composites.

2. Materials

2.1. Mix ingredients

For the modeling of steel fiber reinforced self-compacting concretes, five different mixes were designed using hooked-end long fibers, straight short

Table 1. SFR-SCC mix ingredients (kg for 1m^3).

Materials	C	L5	L10	S5	H10
Portable Water	220	220	220	220	220
Portland Cement	420	420	420	420	420
F-type Fly Ash	180	180	180	180	180
Coarse Aggregate	636	636	636	636	636
Crushed Sand	353	353	353	353	353
Natural Sand	424	424	424	424	424
Steel Fiber	0	39	78	39	78
SP	3.4	3.6	4.2	4.2	4.5

fibers, and hybrid fibers, which consist of straight short fibers and hooked-end long fibers. The maximum steel fiber volume of 1% was selected since the mixes should have adequate flowability and passing ability requirements as well as low cost of the structural elements. Two fiber volumes of 0.5% and 1% were utilized for the long fibrous samples, whilst only 0.5% short fibrous specimens, and 1% hybrid fiber reinforced samples were utilized in the scope of the research. 1% short fibrous mixes could not be produced as self-compacting concrete since balling effect was occurred and the passing ability criteria could not be satisfied for the 1% short FRC during mixing. Table 1 illustrates the ingredients of the five different types of SFRSCC mixes. The non-fibrous or control mix was shown as C, the long fibrous mixes with 0.5% and 1% were indicated as L5 and L10, and the 1% hybrid fibrous mix that includes 0.5% straight short and 0.5% hooked-end long fibers was termed as H10. For the binder materials of the SCC mixes, low calcium fly ash and Ordinary Portland cement were utilized, and the fly ash dosage was set at 30% of the total binder content, as a 30% replacement level was found to be optimal for the mechanical and durability performance [33]. For the water to cement ratio calculations, a k_f factor of 0.4 was utilized for the fly ash in accordance with BS EN 2016 standard [34].

In this research, two types of steel fibers were utilized: hooked-end long fibers and straight short fibers. The hooked-end steel fibers were 35 mm in length having a diameter of 0.55 mm, resulting in an aspect ratio of 64, whereas the straight short fibers were significantly shorter and thinner, with a length of 13 mm and a diameter of 0.16 mm, providing a higher aspect ratio of 81. In terms of tensile strength, the hooked-end long steel fibers showed a higher value of 1345 MPa compared to 1100 MPa for the straight short steel fibers. It should be noted that hooked-end long fiber tensile strength was slightly better than the tensile strength of short fiber.

The low calcium (F-type) fly ash with a density of 2.13 and CEM I 42.5 R cement with a density of 3.14 were used as binder materials. Table 2 shows the physical properties and chemical composition of the cement and fly ash materials. Coarse aggregate with a maximum grain size of 10 mm, crushed and natural sands were used with densities of 2.74, 2.60 and 2.68 g/cm^3, respectively. Grading curves and sieve analysis of aggregates were given in Fig. 1 and Fig. 2. Polycarboxylic ether-based superplasticizer with a density of 1.1 g/cm^3 was utilized to achieve self-compacting concrete requirements without bleeding and segregation.

2.2. Mixing procedure

During mixing, aggregate and binder materials were included and mixed at 2 min in a mixer. Then, the water and superplasticizer were mixed in a container and the obtained liquid was included in 1 min to the mixer and the mix was also mixed additional 1 min. After, steel fibers were incorporated to the mixer in 1 min and then the fibrous mixes were further mixed additional 1 min for the steel fibrous mixes, whilst mixes without steel fibers were also mixed at 2 min to obtain same mixing procedure with steel fibrous specimens. This procedure was finished within 6 min.

2.3. SFR-SCC specimens for modeling

In the scope of the model research, prismatic flexural specimens were casted and tested under three-point bending tests to obtain force versus crack opening displacement curve required for the characterization of tensile stress-strain data of the steel fibrous specimens. For this purpose, control (no fiber), L5 (0.5% long SFR-SCC), L10 (1% long SFR-SCC), S5 (0.5 % short SFR-SCC), H10 (0.5% short and 0.5% long SFR-SCC) specimens were cast and tested under three-point bending. The sizes of the specimens were selected as 150 (width) x 150 (depth) x 600 (length) mm conforming to EN 14651 standard [35]. In addition, 100 mm x 200 mm cylinder samples were also produced to find out splitting tensile strength and elastic modulus, and 150 mm x 150 mm x 150 mm

Table 2. The physical properties and chemical composition of the cement and fly ash.

Material	SiO_2 (%)	Al_2O_3 (%)	CaO (%)	Fe_2O_3 (%)	MgO (%)	SO_3 (%)	Na_2O (%)	K_2O (%)	Cl (%)	LOI	Specific Gravity (g/cm^3)
Cement	19.63	5.58	63.67	3.32	1.25	3.23	0.21	0.68	0.04	2.03	3.14
Fly Ash	54.76	25.26	2.10	6.28	2.08	0.2	0.38	4.04	0.01	3.30	2.13

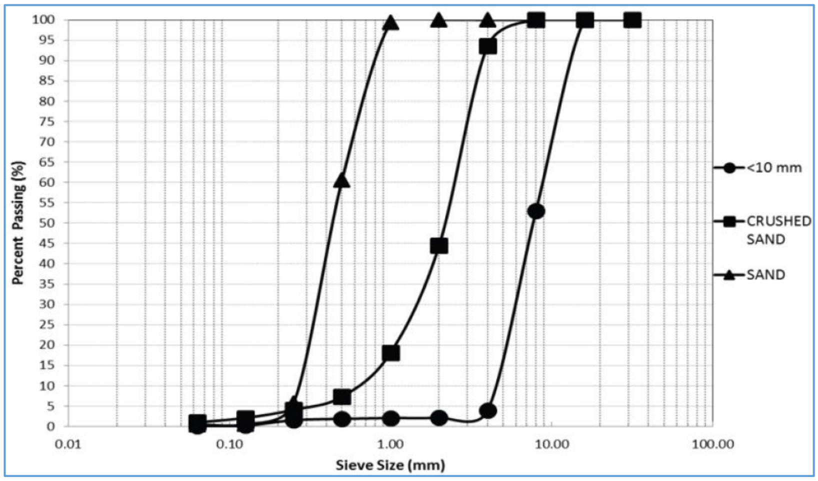

Fig. 1. Grading curves of the aggregates.

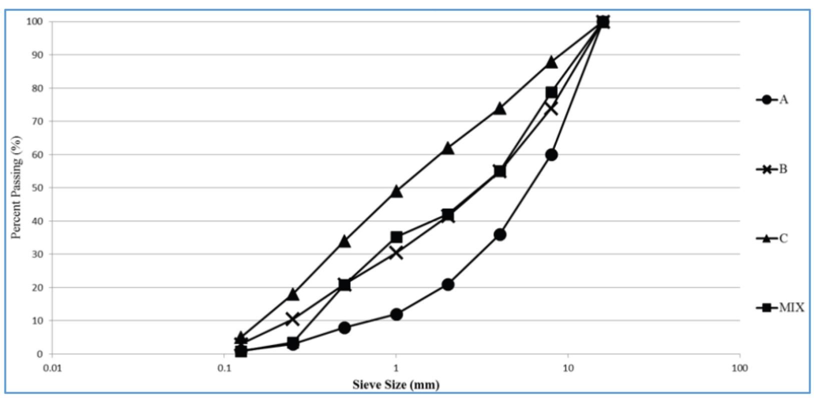

Fig. 2. Sieve analysis of the used aggregates.

cube specimens were also cast to obtain compressive strength of the SFR-SCC specimens required for the inverse modeling.

2.4. Casting and curing of specimens

For the better alignment of the steel fibers in the casting direction, the SFR-SCC mixtures were cast to the molds from one side and left to flow to the other side under its own-weight without any vibration. After 24h, the SFR-SCC samples were demolded and put in the water with 20 ± 2 °C for 28d to gain adequate strength before the execution of the mechanical strength tests.

3. Experimental program

3.1. Tests on fresh concrete properties

Tests on fresh concrete properties were realized to evaluate the required characteristics of the SFR-SCC mixtures according to the related standards as given in Table 3.

Table 3. Fresh-state testing and related standards.

Fresh State Tests	Measured Value	Related Standard
Slump Flow	t_{500} (s) t_{final} (s) flow (cm)	EN 12350-8 [36]
J-Ring	t_{500} (s) t_{final} (s) flow (cm) PJ (cm)	EN 12350-12 [39]
L-Box	PL (H2/H1)	EN 12350-10 [38]
U-Box	H1-H2 (cm)	UNI 11044 [40]
V-Funnel	t_v (s)	EN 12350-9 [37]

3.2. Force controlled compressive and splitting tensile strength tests

For the cube compressive strength data required for the model (f_{cmax}), 150 mm x 150 mm x 150 mm cubic samples were tested under force-controlled loading

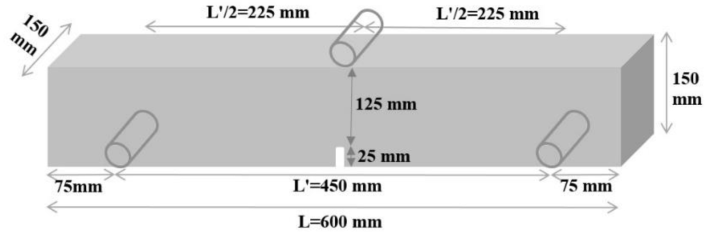

Fig. 3. Three-point loading scheme.

with a rate of 13.5 kN/s in accordance with EN 12390-3 standard [41]. Also, splitting tensile strength tests were executed on 100 mm x 200 mm cylinder samples conforming to ASTM C496/C496 M-11 standard [42] to obtain splitting tensile strength ($f_{ct,splt}$) data required for the inverse model. Three cube samples for the force-controlled compressive strength and three cylinder samples for the splitting tensile strength were tested for the average values.

3.3. Displacement-controlled uniaxial compression test

Displacement-controlled uniaxial compression tests were also realized on 100 mm x 200 mm cylinder samples to obtain required input parameters of elastic modulus (E), linear elastic strain (ϵ_{co}) and ultimate strain (ϵ_{cmax}) for the inverse modeling. To monitor specimen deformation, two Linear Variable Displacement Transducers (LVDTs) were mounted on the cylindrical samples. Three cylindrical fibrous samples were tested for each series using MTS closed-loop test machine and stress versus strain data were obtained.

3.4. Flexural strength test

The accuracy of the predicted inverse models has to be checked by flexural strength tests; therefore, three-point bending tests on each SFR-SCC prismatic notched specimens were executed. By three-point bending tests, force versus crack mouth opening displacement (CMOD) curves were obtained for each fiber reinforced concretes and these obtained curves were compared with the predicted/formed models using input parameters. Fig. 3 illustrates three-point bending test set-up for the SFR-SCC specimens. For each steel fibrous series, 2 companion specimens were produced and tested conforming to EN 14651 standard [35]. In general, three specimens were cast to obtain the average value of companion specimens. However, for the flexural strength tests, the specimen dimensions were 150 × 150 × 600 mm (13.5 L per specimen), while the concrete mixer capacity in the laboratory was 32 L. Therefore, only two companion specimens could be produced in a single mixing batch. A notch was formed in the middle of the 150 mm x 150 mm x 600 mm beam specimens at the bottom part (tension region) with a width of 4 mm and height of 25 mm. Also, the shear span to depth ratio (a/d) ratio was of 1.5 and clear specimen height was 125 mm as shown in Fig. 3.

Three-point bending tests were carried out using an MTS testing machine under crack mouth opening displacement (CMOD) control. Two CMOD paces of 0.05 mm/min and 0.2 mm/min were used during testing procedure. The CMOD rate of 0.05 mm/min were used from 0 - 0.1 mm CMOD, and the CMOD rate further increased to 0.2 mm/min after 0.1 mm to 4 mm CMOD based on the EN 14651 standard [35]. The bending tests automatically terminated when CMOD value became 4 mm for all SFR-SCC specimens. Four LVDTs (two lateral and two vertical) were employed to record the CMOD and vertical deformations throughout the experiment, in addition to the CMOD gauge. The CMOD device was installed at the lower part of the fibrous samples, directly at the notch-tip, as illustrated in Fig. 4. Horizontal LVDTs were used alongside the CMOD gauge to verify and cross-check the crack opening measurements obtained from the CMOD device.

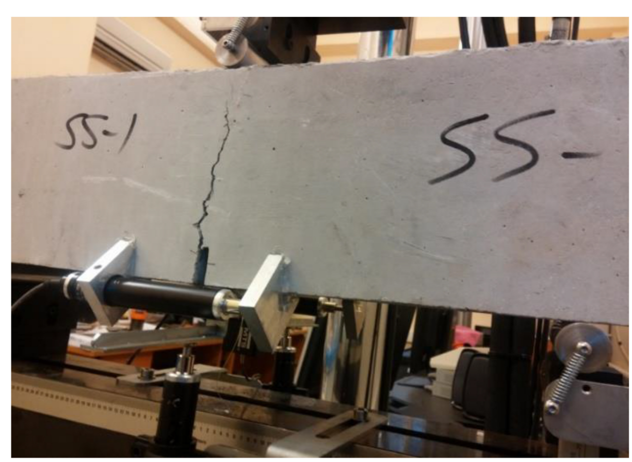

Fig. 4. CMOD controlled flexural loading.

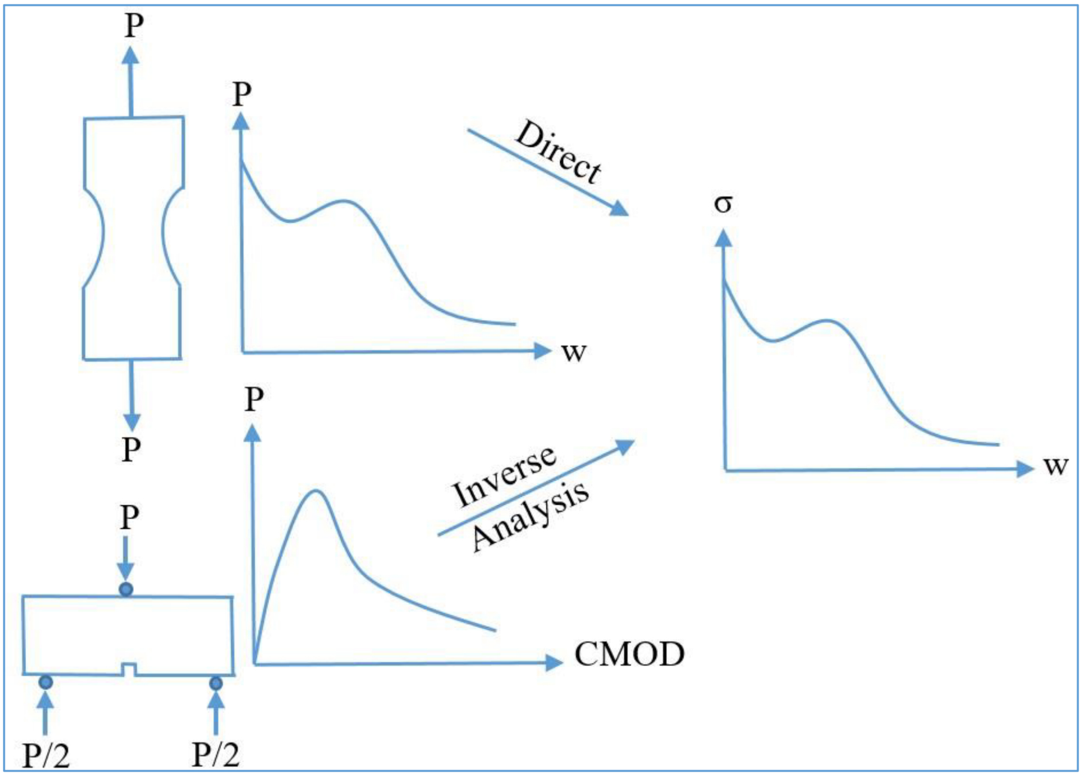

Fig. 5. Tensile characteristics of SFRC (using inverse analysis).

4. Simulation of flexural behavior in SFR-SCC

The limited adoption of steel fibre-reinforced concrete in structural design practice is primarily attributed to the absence of well-defined tensile stress–strain characteristics for fiber-reinforced concretes. The primary advantages of steel fibres include increased residual tensile resistance and improved ductility, which are largely governed by their in strict characteristics. The tension response of fibrous samples is commonly governed via a stress vs strain (σ–ϵ) law prior to matrix cracking, while after cracking it is more appropriately expressed in terms of stress versus crack opening displacement (σ–COD). The σ–COD relationship can be determined directly through a uniaxial direct tensile test; however, this method is costly and requires specialized testing equipment [43]. Alternatively, it may be derived indirectly by performing an inverse analysis based on three- or four-point flexural tests, as illustrated in Fig. 5.

Several inverse (multilayer) modelling approaches have been proposed to support the structural design of fibre-reinforced concretes [29–32, 44–47]. There is still no general standard for direct determination of stress versus crack opening relationships, and different models exist in literature with different degree of accuracy and complexity. Nevertheless, previous studies have demonstrated that the existing models are unable to accurately predict the tensile response of a wide range of fibre-reinforced materials, which has hindered their broader adoption in structural design. Consequently, further refinement of current models and/or the development of new approaches is required. Although, researchers focus on the characterization of steel fiber reinforced concretes using three-point bending tests, there is still limited investigation expressing the significance of applying a suitable testing method to characterize steel fiber reinforced concrete for a safe structural member design, especially for the self-compacting concrete members [27]. In this research, the equilibrium-based multilayer approach is adopted and further modified for long SFR-SCC materials and new input parameters were proposed in the literature for the short and hybrid fibrous concretes.

4.1. General approach of the multi-layer model

During an experiment of a notched beam under 3-point bending test, maximum moment arises at mid-point of the bottom part of the specimens and crack emerges through the notch plane. A non-linear hinge is formed at middle portions with a length of l_f

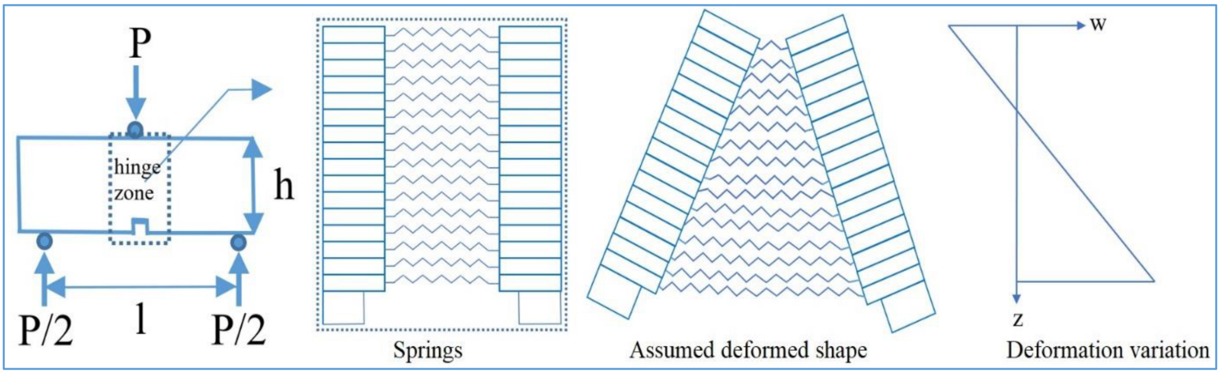

Fig. 6. Incremental procedure of inverse analysis - springs and deformation variation.

as indicated in Fig. 6. The l_f length was taken as half of the effective beam height, which was determined after numerous simulations [48]. The remained or out of the hinge zone is accepted as elastic. This hinge behaves as linear elastic up to the crack initiation, then the behavior becomes non-linear. Therefore, this hinge portion can be modeled by layers of springs, whose behavior is governed by the tensile constitutive relations of fibrous concrete, demonstrating the influence of steel fiber yielding and pull-out. The crack opening profile is linear in this hinge zone [49].

The fracture characteristics can be found by an inverse analysis based on non-linear hinge model to achieve the significant requirements of the bilinear tension softening diagram [4]. The equilibrium-based multi-layer, an inverse analysis, method depends on 3 fundamental principles as described in the earlier inverse analysis model studies [29–32]. In the initial approach, the prismatic beam sample is divided into two segments which are then interconnected by springs distributed along the effective height of the beam, as illustrated in Fig. 6. This spring region (hinge region, representing non-linear behavior) comprises of multiple layers and each one shows the small layer behaviors. As the number of layer is increased, the model accuracy is increased, and a linear displacement distribution over the beam depth is anticipated. The fracture, or non-linear hinge zone, governs the overall flexural response of the beam. In this approach, the beam is assumed to be infinitely stiff outside the fracture zone.

In the second approach [29–32], strains in springs or concrete layers correspond to the average strain distribution of that layer. The corresponding stresses were calculated for each layer from the strain distributions, thus stress-strain and stress-COD relations were obtained as an input parameter for the model. Based on the computed stresses, the bending moment is first determined for each individual layer and then summed over the entire cross-section, ensuring that the resultant force is equivalent to zero using 1st and 2nd equations, which are the equilibrium conditions of the model (Fig. 7). After the determination of the bending moments, applied load is calculated by three-point bending formula by 3rd equation.

$$N = \sum_{i=1}^{i=n} \sigma_i x \; b \; x \; h_i = 0 \tag{1}$$

$$M_{int} = \sum_{i=1}^{i=n} \sigma_i x \; b \; x \; h_i \; x \; z_i = 0 \tag{2}$$

$$P = 4 \; x \; \frac{M}{L} \tag{3}$$

In the third and the latest approach; an incremental process is done to find complete load crack mouth opening displacement (P-CMOD) curves. In the first step, the strain at the bottom layer is prescribed at a fixed value. The linear strain distribution across the section is then obtained using equilibrium conditions until the resultant normal force becomes zero. Subsequently, the bottom layer strain is enhanced incrementally, and the highest tension and compression strains, along with the equivalent bending moments, are found at each step. The global load–displacement (P–w) curve is then constructed by combining the applied load and the associated displacement for every increment, as illustrated in Fig. 8. Finally, the predicted response of the model is compared with the experimental results to evaluate its accuracy [29–32].

4.2. General model parameters

4.2.1. Number of layers and influence length

The number of layers (n) in the hinge zone influenced the peak load in the model. Similar with finite element analysis, the model accuracy was improved with an increase in the number of layers. However,

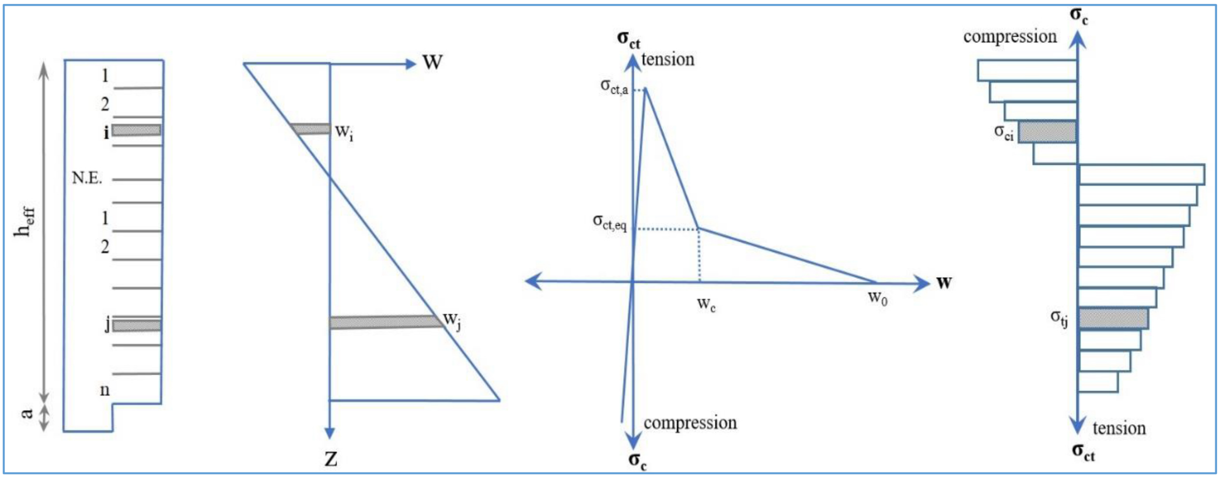

Fig. 7. Incremental procedure of inverse analysis – section analysis using slices.

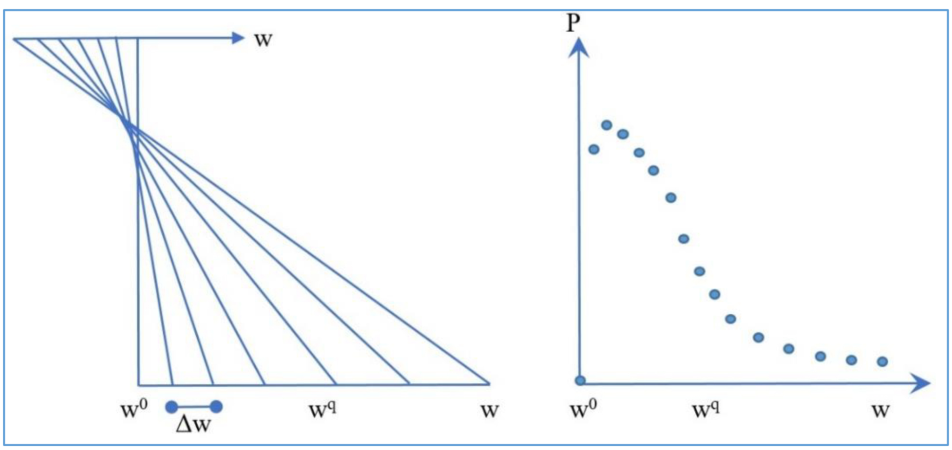

Fig. 8. Last step of multi-layer procedure.

as the number of layers increased, the analysis time of the model is extended. In the earlier investigation, it was reported that the number of layer of 500 was found adequate and further increase in the number of layers did not change the peak load. Also, the influence length or hinge zone also was also taken as half of the effective beam depth for the representation of the non-linear behavior [30]. The similar number of layers (500) and influence length ($h_{effective}/2$) were also utilized in the previous model studies [31, 32]. Therefore, the number of layer and influence length were also used as 500 and 62.5 mm ($h_{effective}/2$), respectively for the input parameters in this study.

4.2.2. Stress versus strain behavior under compression

One of the important parameters to obtain an accurate tensile stress-strain model is the utilization of reliable stress versus strain data under compression as an input parameter. In the previous research, three different stress-strain data were utilized to represent the best input parameter for the simulation of the inverse modeling and the idealized stress versus strain relationship under compression as shown in Fig. 9 was found the best behavior representing the tensile stress-strain relationship of the specimens [30]. The idealized stress-strain behavior was also utilized in the previous model investigations [31, 32]. In this research, the same stress-strain response was used as an input parameter as shown in Fig. 7.

For the determination of the f_{cm}, $\epsilon_{c,elastic}$ and $\epsilon_{c,max}$ values in the Fig. 9, Kooiman [30] was realized the compressive strength test experiments and the experiment findings were utilized as input parameters for the inverse approach. The compressive strengths of the fibrous samples was used as input parameters for the inverse model. The compressive strength results were obtained from force-controlled loading on 150 mm x 150 mm x150 mm cube specimens, whilst the elastic modulus (E), linear elastic strain limit ($\epsilon_{cc,elastic}$) and ultimate limit strain ($\epsilon_{cc,max}$) values

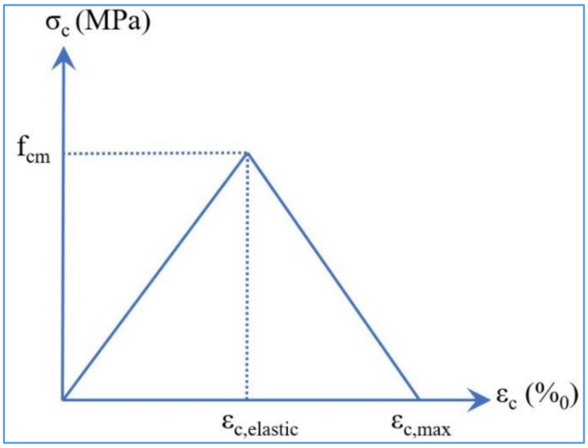

Fig. 9. Idealized compressive stress - strain behavior.

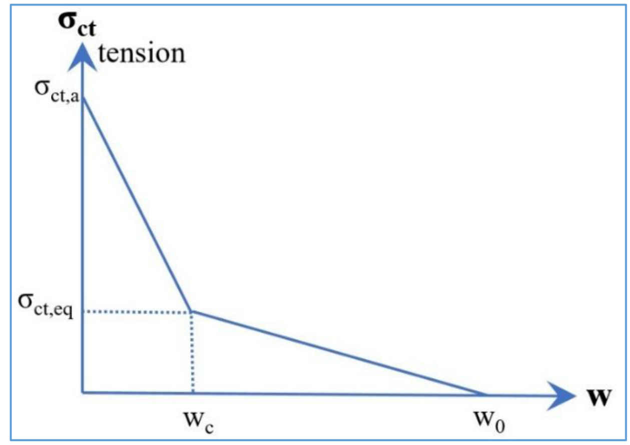

Fig. 10. Input parameters for post cracking behavior of SFRC.

were obtained from displacement controlled compressive strength tests conducted on 100 mm x 200 mm cylindrical specimens.

4.2.3. Stress-strain relationships

The fracture parameters were accurately predicted using inverse modeling to reach the fundamental parameters of bilinear tension softening curve. In this curve, stress-strain and stress-crack width relationships can be separated into 2 fragments: the linear portion up to cracking and the softening fragment. The elastic performance was estimated by uniaxial tensile strength ($\sigma_{ct,a}$) and linear elastic strain (ϵ_{ct}). The softening was also estimated using critical crack width (w_0), uniaxial tensile strength ($\sigma_{ct,a}$), characteristic crack width (w_c) and the equivalent post cracking strength ($\sigma_{ct,eq}$) parameters as shown in Fig. 10.

The predicted value of uniaxial tensile strength ($\sigma_{ct,a}$) was correlated with the experimental splitting tensile strength test results ($\sigma_{ct,splt}$). The critical crack width (w_0) generally impacts the displacement part in the post-cracking region and the w_0 value varies according to steel fiber length; therefore, the predicted value of critical crack width (w_0) was correlated with the steel fiber length (F_L). Also, the estimated value of characteristic crack width (w_c) influences the crack opening displacement region and the w_c value also depends on the steel fiber length. Thus, characteristic crack width (w_c) value was correlated with the critical crack width (w_0) value, depending on the length of the steel fibre. Meanwhile, the corresponding post-cracking strength ($\sigma_{ct,eq}$) influences the stress part and the $\sigma_{ct,eq}$ value was related to the uniaxial tensile strength ($\sigma_{ct,a}$). The predicted input parameters depending on the steel fiber length and splitting tensile strength values were given in Table 7 after the completion of the required deviation checks between model and experimental tests results.

4.3. Determination of model accuracy

Model simulations were executed for various SFR-SCC specimens and iteratively repeated up to the variance between the experimental and numerical results fell below 5% for each of the four criteria described herein. The determination of the model accuracy is checked based on the previous studies [29–32], which were chosen as reference values for the evaluation of the model results with the experimental outcomes. For this purpose, the below checks are satisfied:

- The highest bending force (P_{max}) difference between model/experiment has to be smaller than 5%.
- The $0.75P_{max}$ flexural load difference (in the post-peak region) between model/experiment has to be smaller than 5%.
- The difference in the toughness value corresponding to 4 mm CMOD value between model/experiment has to be smaller than 5%.
- The difference in toughness values between the experimental outcomes and the model expectations, calculated at a CMOD value matching to 75% of the highest experimentally found bending force (at post-peak zone), must be less than 5%.

4.4. Multilayer model procedure

Multilayer (inverse) model procedure was summarized below. After the generated simulation, model accuracies were checked according to the rules given in Section 4.3. If deviation amount smaller than the 5%, the input parameters become the final param-

Table 4. Flowability and passing ability findings.

SCC Tests		C	L5	L10	S5	H10	Standards and Limit Values
Slump Flow	t_{500} - s	2	3	4	4	5	EN 12350 - 8 t_{500}: 0-6 s flow > 60 cm
	t_{final} - s	13	15	19	17	19	
	flow - cm	79	79	80	79	75	
J Ring	t_{500} - s	3	4	5	5	7	EN 12350 - 12 PJ≤2
	t_{final} - s	19	19	21	21	23	
	flow - cm	73	69	68	69	60	
	PJ - cm	0.1	1.8	2.1	2.0	3.4	
L Box	$PL=H_2/H_1$	1.00	0.96	Congestion	0.94	Congestion	EN 12350 - 10 $H_2/H_1 \geq 0.8$
U Box	H_1 - H_2 (cm)	0.6	1.4	Congestion	1	Congestion	UNI 11044 H_1 - H_2 < 3 cm
V Funnel	t_v - s	5	6	Congestion	6.5	Congestion	EN 12350 - 9 t_v < 15 s

eters of tensile stress versus strain relationship of SFR-SCC. If the deviation amount higher than the 5%, then input/predicted parameters were changed in the models up to the deviation amount becomes smaller than 5% as explained in the below steps. Final parameters were accepted as the tensile stress-strain relationship of the SFR-SCC. The multilayer model (inverse analysis) procedure steps are [29–32]:

i. Use the input values required for the inverse analysis. The experimentally determined values of compressive strength (f_c), linear elastic strain limit (ϵ_{c0}), elastic modulus (E), ultimate limit strain (ϵ_{cmax}) from compressive strength tests, and splitting tensile strength values ($f_{fctm,splt}$) from splitting tensile strength tests for each fibrous concretes were utilized in the models.
ii. Assume number of layers and influence length parameters. These parameters are kept constant as 500 and 62.5 mm, respectively.
iii. Assume bilinear stress-crack with relation parameters of uniaxial elastic tensile strength and strain ($f_{fctm,ax}$ and ϵ_{ct}), equivalent post cracking tensile strength ($f_{fctm,eq,bil}$), and characteristic and critical crack widths (w_0 and w_c).
iv. Assume a CMOD value at the notch level.
v. Calculate deformations of each layer and convert them to the strains using equilibrium equations.
vi. Iterate strain values step by step and find out the corresponding moment values (2nd equation)
vii. Find out the load value by 3rd formula.
viii. Increase the selected CMOD value at step iv and repeat the steps from v-vii to obtain overall load versus CMOD curve as shown in Fig. 6.
ix. Compare the model predictions with the experimental results and determine the deviation among the experimental outcomes and theoretical findings. If satisfies the criteria, then the model is accurate. If not, change the assumed parameters in step iii and repeat the following steps up to the satisfaction of the criteria given in Section 4.3.

5. Results and discussions

5.1. Fresh state test results

Table 4 presents the fresh-state testing results. Slump flow properties were found satisfactory according to EN 12350-8 standard [36]. J-Ring results indicated that mixes except for the hybrid mix showed adequate passing ability (PJ≤2) conforming to EN 12350-12 standard [39]. L-Box test indicated that control and 0.5% SFR-SCC mixes were found satisfactory (PL≥0.8) according to EN 12350-10 standard [38]; but, blocking was detected on 1% fibre-reinforced mixtures. Similar findings were also observed for U-Box and V-Funnel tests in accordance with UNI 11044 [40] and EN 12350-9 [37] standards, respectively.

The flowability results showed that L10 samples contained a higher amount of superplasticizer (4.2 kg/m^3) than the L5 samples (3.6 kg/m^3); therefore, the L10 mixtures exhibited a more workable consistency and higher flowability than the L5 mixtures. Although the S5 and L10 samples had similar superplasticizer contents (4.2 kg/m^3), the S5 samples showed lower workability and reduced flowability due to the increased internal friction caused by the higher number of short fibers.

In these tests, control and 0.5% fiber reinforced mixes showed adequate passing ability; however, blocking was observed for higher amount of steel fibrous mixes (1%). The clear spacing between the steel bars in the L-Box and U-Box arrangements is 40 mm, while the long-fibres had of 35 mm length. Hence, when high fibre volume fractions were employed, fibre accumulation and blockage around the steel bars were expected. However, it should be noted that these tests are applicable for the plain (non-fibrous) SCC mixes, there is no suggestion exist in the literature

Table 5. 28-day compressive and splitting tensile strength results.

Samples	Compressive Strength Test (28th day) (MPa)	Splitting Tensile Strength Test (28th day) (MPa)
C (Non-fibrous)	57.75	4.14
L5	59.23	4.35
S5	58.92	4.67
L10	61.98	7.57
H10	61.18	6.39

Table 6. Displacement controlled test parameters of SFR-SCC for modeling.

Concrete	Elastic Modulus (E) (MPa)	Linear Elastic Strain Limit ($\epsilon_{c,elastic}$)	Ultimate Strain Limit ($\epsilon_{c,ultimate}$)
Long (0.5 %)	31217	0.0017	0.01
Short 0.5 % FRC	30323	0.0026	0.015
Long (1%) FRC	36319	0.003	0.015
Hybrid (1%) FRC	36817	0.004	0.015

for the flowability and passing ability requirements of the fiber reinforced mixes. The detailed evaluation of the fresh state properties of the SFR-SCC mixes was also reported in the earlier investigation [18].

5.2. Compressive and splitting tensile strength test results

Table 5 illustrates the average compressive and splitting tensile strength results. It should be noted that these results were used as input values in the modeling phase. The results showed that both compressive and splitting tensile strengths of the specimens enhanced with an increasing steel fiber volumes. The slight compressive strength improvements of 6% for 1% long and 7% for 1% hybrid steel fiber introductions, whilst significant splitting tensile strength enhancement of 83% for 1% long and 55% for 1% hybrid steel fiber inclusions were observed at 28 days. The 0.5 % steel fiber inclusions had found very limited impact on the both compressive and splitting tensile strength results at the age of 28 days.

5.3. Displacement controlled compressive strength test results

Table 6 summarizes displacement controlled compressive strength results, and elastic modulus (E), linear elastic strain limit ($\epsilon_{cc,elastic}$) and ultimate limit strain ($\epsilon_{cc,max}$) values were find out for each fibrous

Table 7. Input parameters of multilayer approach.

General Model Parameters		Steel fibrous specimens: L5 0.5 % Long SFR-SCC	S5 0.5 % Short SFR-SCC	L10 1 % Long SFR-SCC	H10 1 % Hybrid SFR-SCC
Number of layers		500	500	500	500
Influence length, 0.5*hlig (mm)		62.5	62.5	62.5	62.5
Bilinear compressive relation		**Input parameters for compression (experimentally found)**			
Compressive Strength (MPa)	f_c	59.23	58.92	61.98	61.18
Linear elastic strain limit (strain)	ϵ_{c0}	0.0017	0.0026	0.003	0.004
E-Modulus (MPa)	E	31160	30853	36319	36817
Ultimate limit strain (strain)	ϵ_{cmax}	0.01	0.015	0.015	0.015
Bilinear stress-crack width relation		**Input parameters for tension**			
Splitting tensile strength (MPa)	$\sigma_{ct,splt}$	4.35	4.67	7.57	6.39
Uniaxial elastic tensile strength (MPa)	$\sigma_{ct,a}$	3.26 ($\sigma_{ct,splt}$ *0.75)	3.50 ($\sigma_{ct,splt}$ *0.75)	5.68 ($\sigma_{ct,splt}$ *0.75)	5.11 ($\sigma_{ct,splt}$ *0.75)
Uniaxial elastic tensile strain (strain)	ϵ_{ct}	0.0001047 ($\sigma_{ct,a}$/E)	0.0001047 ($\sigma_{ct,a}$/E)	0.0001563 ($\sigma_{ct,a}$/E)	0.0001389 ($\sigma_{ct,a}$/E)
Equivalent post cracking tensile strength (MPa)	$\sigma_{ct,eq}$	0.9787 ($\sigma_{ct,a}$ *0.3)	1.5761 ($\sigma_{ct,a}$ *0.45)	1.7032 ($\sigma_{ct,a}$ *0.3)	2.0448 ($\sigma_{ct,a}$ *0.4)
Critical crack width (mm)	w_0	11.55 (0.33*F_L)	6.5 (0.5*F_L)	11.55 (0.33*F_L)	11.55 (0.33*F_L)
Characteristic crack width (mm)	w_c	2.8875 (w_0/4)	1.3 (w_0/5)	2.8875 (w_0/4)	2.8875 (w_0/4)

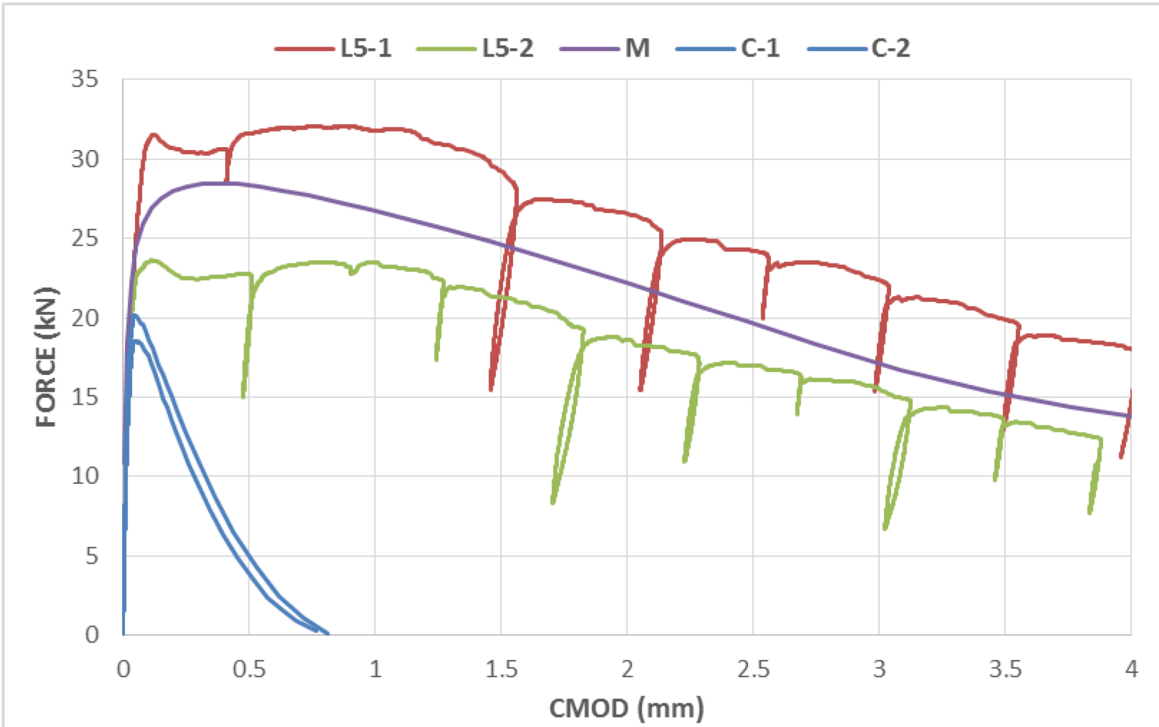

Fig. 11. Experiment and Model (M) outcomes of L5 samples (0.5%-long).

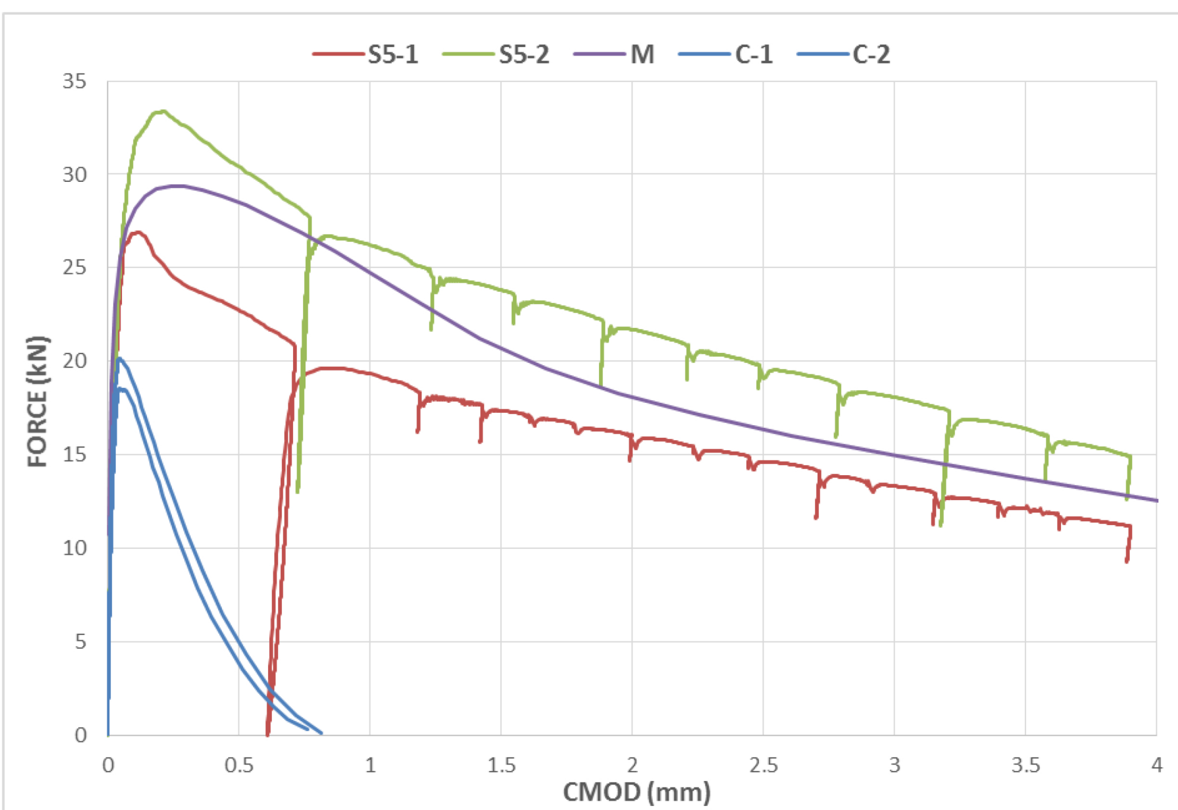

Fig. 12. Experiment and Model (M) outcomes of S5 samples (0.5%-short).

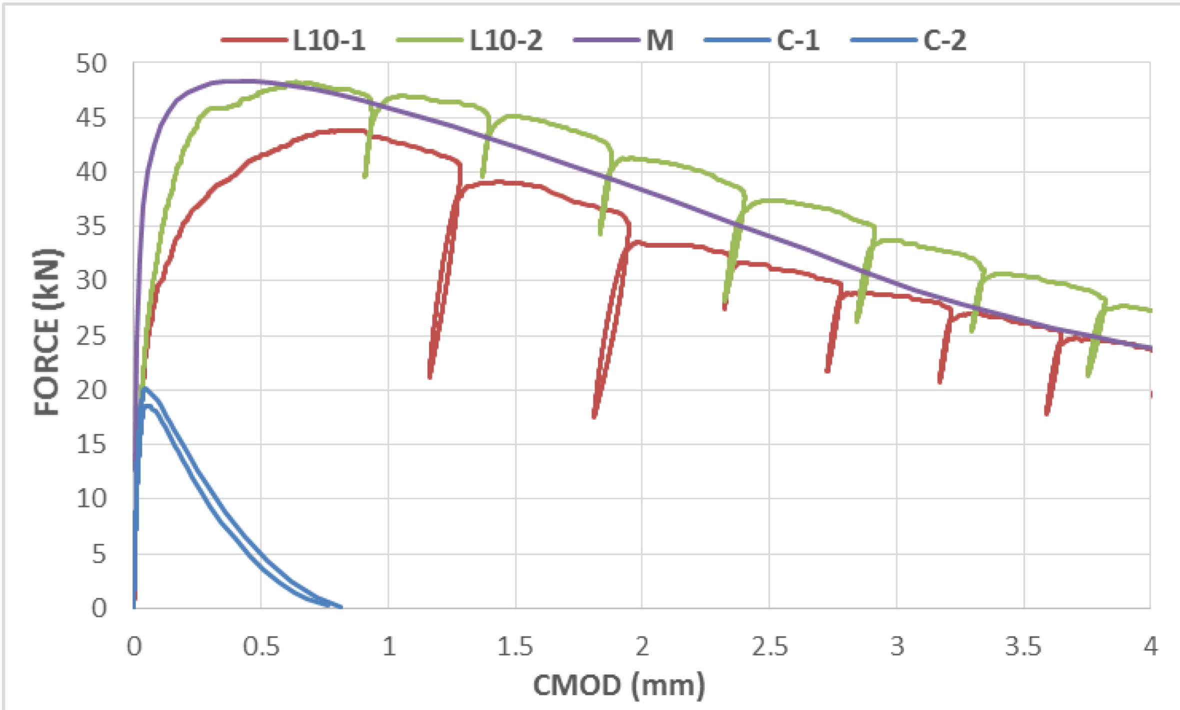

Fig. 13. Experiment and Model (M) outcomes of L10 samples (1%-long).

concretes required for the inverse analysis. In addition, the average elastic modulus of the non-fibrous specimens was obtained as 28823 MPa. The results indicated that the elastic modulus of SFR-SCC increased slightly with increasing steel fibre content. Similar findings have also been reported in the literature [50, 51]. For the modeling, these parameters only contribute to the slope of the pre-peak region of the force versus crack mouth opening displacement (CMOD) curve.

5.4. Three-point flexural strength tests and model results

The aim of the study was to predict direct tensile stress-strain diagrams. For this reasons, compressive and splitting tensile strength tests, which are easier to perform, were executed to use input parameters required for the modeling of direct tensile stress versus strain curve of SFR-SCC. The accuracy of the inverse model results has to be checked for the standardization of direct tensile stress-strain curve of the SFR-SCC for the material characterization. For this aim, three-point flexural strength tests on notched specimens were carried out to check the experimental results with the inverse analysis model simulations. After trial simulations and deviation checks, the inverse models were successfully composed for each SFR-SCC specimens and Table 7 illustrates the final model parameters. Figs. 11 to 14 show the composed model (M) results with the flexural strength test results and the final input parameters were deemed satisfactory once the deviation between the experimental and theoretical curves was confirmed to be within 5%. After model simulations, the uniaxial elastic tensile strength was found 0.75 times the splitting tensile strength for all fibrous samples. The equivalent post cracking tensile strength was obtained as 0.3 times the uniaxial elastic tensile strength for 0.5% and 1% long fibrous specimens, and 0.4 times the uniaxial elastic tensile strength for 1% hybrid fibrous and 0.45 times the uniaxial elastic tensile strength for the 0.5% short fibrous specimens. The critical crack width values for the 0.5% long, 1% long and 1% hybrid fibrous specimens were found to be 0.33 times the steel fiber length, and 0.5 times the steel fiber length for the 0.5% short fibrous specimens. The characteristic crack width (w_c) values were obtained as critical crack width (w_0)/4 for 0.5 long, 1% long and 1% hybrid fibrous specimens, and w_0/5 for 0.5% short fibrous specimens as indicated in Table 7. The results pointed out that tensile stress-strain response was significantly influenced from the steel fiber type. For the hybrid fibrous specimens, the behavior of long fibers was found dominant on the response since similar assumed parameters were utilized in the long and hybrid fibers, except for only the equivalent post cracking tensile strength.

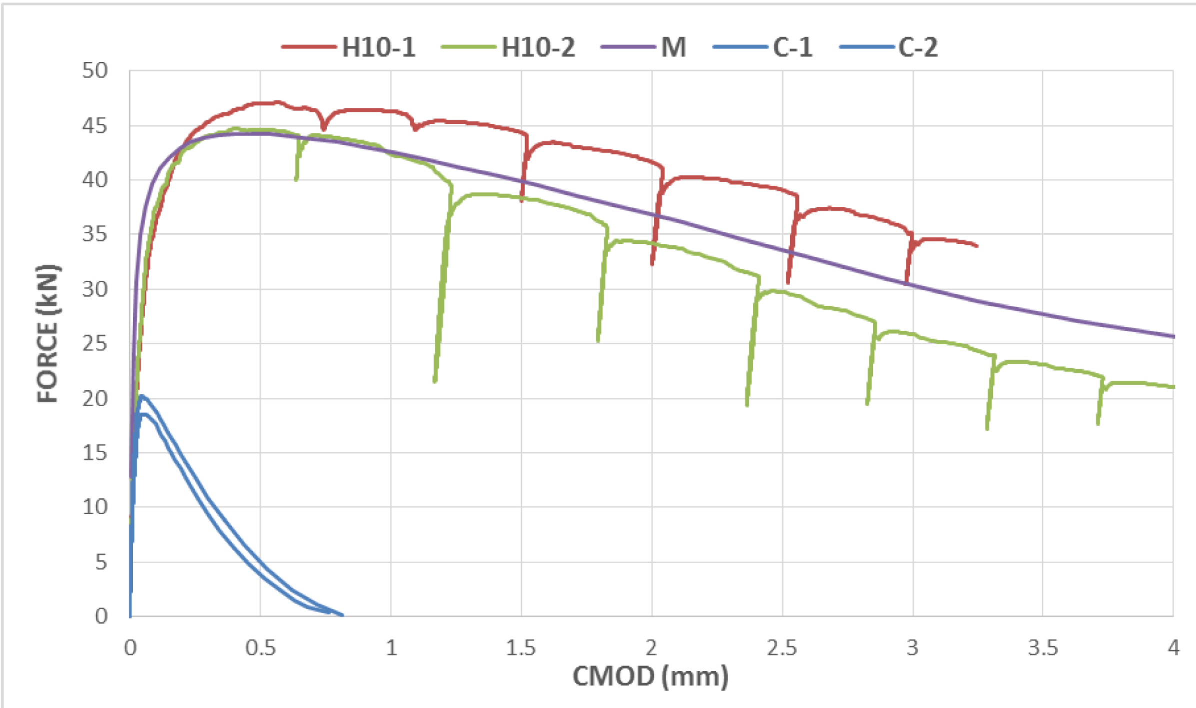

Fig. 14. Experiment and Model (M) outcomes of H10 samples (1%-hybrid).

Table 8. Tensile input parameters for the modelling.

Input parameters	Current study	Kooiman [30]	Grünewald [31]
$\sigma_{ct,a}$	$\sigma_{ct,splt}$ *0.75	0.7-0.8* $\sigma_{ct,\ split}$	0.45-0.68* $\sigma_{ct,\ split}$
$\sigma_{ct,eq}$	0.3* $\sigma_{ct,\ a}$ (L5, L10) 0.4* $\sigma_{ct,\ a}$ (H10) 0.45* $\sigma_{ct,\ a}$ (S5)	0.2-0.3* $\sigma_{ct,a}$	0.2-0.35* $\sigma_{ct,a}$
w_0	0.33*F_L (L5, L10, H10) 0.5* F_L (S5)	0.33-0.425* F_L	0.26-0.42* F_L
w_c	0.25*w_0 (L5, L10, H10) 0.2* w_0 (S5)	0.17-0.2* w_0	0.22-0.36* w_0

Figs. 11 to 14 illustrate the force versus crack mouth opening displacement (CMOD) relations. The reason of the sharp decrease in the load resulted from the CMOD controlled loading. Non-fibrous SCC specimens were also given to observe the steel fiber efficiency. It can be concluded that steel fibrous specimens with high volume (1%) have higher flexural strength and residual flexural strength capacity compared to lower amount steel fibrous specimens, as expected. The effect of the steel fibers especially on the post-peak performance was obvious.

5.4.1. Contributions to the multi-layer model in this research

In the research, similar method as reported by Kooiman [30] and Grünewald [31] was utilized to find out the input parameters; however, further modification was made for modeling of the long fibrous specimens. For long FRC specimens, the input parameters were close to the parameters of Kooiman rather than Grünewald. However, Kooiman estimated low characteristic crack width (w_c) values for long FCR specimens. In addition to this, for the short and hybrid fibre-reinforced samples, novel input parameters were successfully found and utilized. The results showed that short-fibrous samples had marginally more $f_{fctm,eq,bil}$ and w_0 values than the long-fibrous samples. Finally, each model was successfully composed for different fiber reinforced concrete specimens. The used parameters of Kooiman, Grünewald and current study for tensile behavior of SFRC were given in Table 8 for model comparison.

6. Conclusions

The main findings of the study were:

- Successful modelling outcomes were achieved for all fibrous samples.
- The utilized input parameters were considered acceptable after verifying that the deviations among the experimental and theoretical curves remained within the specified limits.
- The input parameters selected for the long fibre-reinforced specimens were consistent with those reported by Kooiman [30] and Grünewald [31]; however, additional modifications were required.
- No data were found in the literature regarding suitable input values for hybrid and short fibre-reinforced samples. Previous research by Grünewald [31] indicated that the numerical model may not accurately capture the experimental response of specimens reinforced with short fibres, leading to notable deviations. To overcome this limitation, the present study introduces a revised set of input parameters specifically developed for short and hybrid fibre systems, which were then incorporated into the modelling procedure.

For the future studies, material characterizations should be further investigated and modelling studies should be done for developing mathematical equations which may applied to wide variety of materials (different fibers, fiber lengths, fiber geometry, and etc.).

Conflict of interest

The authors declare that they have no known competing financial interests or personal relationships that could have appeared to influence the work reported in this paper.

Author contribution

All of the authors have contributed equally to the article. Further, all of the authors have validated and approved the final manuscript.

Data availability

All graphs and data obtained or generated during the investigation appear in the published article

Funding

None.

References

1. Erdem TK. Use of AlaçatıStone Aggregate in Conventional and Self-Consolidating Concretes. *Journal of Sustainable Construction Materials and Technologies*. 2025;10(4):7.
2. Başsürücü M, Fenerli C, Kına C, Akbaş ŞD. Effect of fiber type, shape and volume fraction on mechanical and flexural properties of concrete. *Journal of Sustainable Construction Materials and Technologies*. 2022;7(3):158–171.
3. Yoo DY, Banthia N. Mechanical properties of ultra-high-performance fiber-reinforced concrete: A review. *Cement and Concrete Composites*. 2016;73:267–280.
4. Ríos JD, Leiva C, Ariza MP, Seitl S, Cifuentes H. Analysis of the tensile fracture properties of ultra-high-strength fiber-reinforced concrete with different types of steel fibers by X-ray tomography. Materials & Design. 2019;165:107582.
5. Niş A, Eren NA, Çevik A. Effects of nanosilica and steel fibers on the impact resistance of slag based self-compacting alkali-activated concrete. Ceramics International. 2021;47(17):23905–23918.
6. Niş A, Eren NA, Çevik A. Effects of recycled tyre rubber and steel fibre on the impact resistance of slag-based self-compacting alkali-activated concrete. European Journal of Environmental and Civil Engineering. 2023;27(1):519–537.
7. Çevik A, Niş A. Introduction to fiber-reinforced alkali-activated composites. In Advanced Fiber-Reinforced Alkali-Activated Composites. 2023:1–21. Elsevier.
8. Gülşan ME, Alzeebaree R, Rasheed AA, Niş A, Kurtoğlu AE. Development of fly ash/slag based self-compacting geopolymer concrete using nano-silica and steel fiber. Construction and Building Materials. 2019;211:271–283.
9. Giaccio G, Tobes JM, Zerbino R. Use of small beams to obtain design parameters of fibre reinforced concrete. Cement and Concrete Composites. 2008;30(4):297–306.
10. Wang XH, Zhang SR, Wang C, Cao KL, Wei PY, Wang JX. Effect of steel fibers on the compressive and splitting-tensile behaviors of cellular concrete with millimeter-size pores. Construction and Building Materials. 2019;221:60–73.
11. Özyurt N, Söylev T, Özturan T, Pehlivan A, Niş A. Corrosion and Chloride Diffusivity of Reinforced Concrete Cracked under Sustained Flexure. Teknik Dergi. 2020;31(6):0–0. DOI: 10.18400/tekderg.430536
12. Ponikiewski T, Katzer J, Bugdol M, Rudzki M. X-ray computed tomography harnessed to determine 3D spacing of steel fibres in self compacting concrete (SCC) slabs. Construction and Building Materials. 2015;74:102–108.
13. Mehta PK, Monteiro PJM. Concrete: Microstructure, properties, and materials. 3rd ed. New York: McGraw-Hill, 2006.
14. Shafigh P, Mahmud H, Jumaat MZ. Effect of steel fiber on the mechanical properties of oil palm shell lightweight concrete. Materials & Design. 2011;32(7):3926–3932.
15. Hassanpour M, Shafigh P, Mahmud HB. Mechanical properties of structural lightweight aggregate concrete containing low volume steel fiber. Arabian Journal for Science and Engineering. 2014;39(5):3579–3590.
16. Li B, Xu L, Shi Y, Chi Y, Liu Q, Li C. Effects of fiber type, volume fraction and aspect ratio on the flexural and acoustic emission behaviors of steel fiber reinforced concrete. Construction and Building Materials. 2018;181:474–486.

17. di Prisco M, Felicetti R, Iorio F, Gettu R. On the identification of SFRC tensile constitutive behaviour. Fracture mechanics of concrete structures. AA Balkema Publishers, Rotterdam. 2001:541–548.
18. Niş A, Özyurt N, Özturan T. Variation of Flexural Performance Parameters Depending on Specimen Size and Fiber Properties. Journal of Materials in Civil Engineering. 2020;32(4):04020054.
19. Baysal A, Yayla P, Türkmen HS. A review on engineering biocomposites and natural fiber-reinforced materials. Journal of Sustainable Construction Materials and Technologies. 2022;7(3):231–249.
20. Gültekin A. Effect of sealed water curing and fiber length on compressive strength and fracture energy of fly ash-based geopolymer mortars. Journal of Sustainable Construction Materials and Technologies. 2024;9(4).
21. Pehlivan AO. Effect of nanosilica addition on the mechanical properties of cement mortars with basalt fibers with or without silica fume. Journal of Sustainable Construction Materials and Technologies. 2022;7(1):17–23.
22. Doğan F, Dehghanpour H, SubaşıS, MaraşlıM. Characterization of carbon fiber reinforced conductive mortars filled with recycled ferrochrome slag aggregates. Journal of sustainable construction materials and technologies. 2022;7(3):145–157.
23. Tiberti G, Minelli F, Plizzari G. Reinforcement optimization of fiber reinforced concrete linings for conventional tunnels. Composites Part B: Engineering. 2014;58:199–207.
24. Rao BK, Ravindra V. Steel Fiber Reinforced Self-Compacting Concrete Incorporating Class F Fly Ash. International Journal of Engineering Science and Technology. 2010;2(9):4936–4943.
25. Abdallah S, Rees DW, Ghaffar SH, Fan M. Understanding the effects of hooked-end steel fibre geometry on the uniaxial tensile behaviour of self-compacting concrete. Construction and building Materials. 2018;178:484–494.
26. Abrishambaf A, Barros JA, Cunha VM. Tensile stress–crack width law for steel fibre reinforced self-compacting concrete obtained from indirect (splitting) tensile tests. Cement and Concrete Composites. 2015;57:153–165.
27. Soltanzadeh F, Cunha VM, Barros JA. Assessment of different methods for characterization and simulation of post-cracking behavior of self-compacting steel fiber reinforced concrete. Construction and Building Materials. 2019;227:116704.
28. Sarmiento EV, Hendriks MAN, Geiker MR, Kanstad T. Modelling the influence of the fibre structure on the structural behaviour of flowable fibre-reinforced concrete. Engineering Structures. 2016;124:186–195.
29. Hordijk DA. Local approach to fatigue of concrete. PhD Thesis, Delft University of Technology, 1991.
30. Kooiman AG. Modelling Steel Fibre Reinforced Concrete for Structural Design. PhD Thesis, Delft University of Technology, 2000.
31. Grünewald S. Performance-based Design of Self-Compacting Fibre Reinforced Concrete. PhD Thesis, Delft University of Technology, 2004.
32. Lappa ES. High Strength Fibre Reinforced Concrete – Static and Fatigue Behaviour in Bending. PhD Thesis, Darmstadt University of Technology, 2007.
33. Imbabi MS, Carrigan C, McKenna S. Trends and developments in green cement and concrete technology. International Journal of Sustainable Build Environment. 2012;1(2):194–216.
34. BSI (British Standards Institution).. Concrete: Specification, performance, production and conformity. BS EN206: 2013 + A1. London: BSI, 2016.
35. EN 14651, Test Method for Metallic Fibered Concrete – Measuring the Flexural Tensile Strength (Limit of Proportionality (LOP), Residual), European Standard. 2005.
36. EN, B. 12350-8. Testing fresh concrete, Part 8: selfcompacting concrete, slump-flow test. British Standards Publication. 2010.
37. EN, B. 12350-9. Testing Self Compacting Concrete: V-Funnel Test. British Standards Publication. 2010.
38. EN, B. 12350-10. Testing fresh self-compacting concrete. L-box test. British Standards Publication. 2010.
39. EN, B.. 12350-12: Testing Fresh Concrete, Part 12: Self-Compacting Concrete, J-Ring Test. British Standards Publication, 2010.
40. UNI 11044, Testing Fresh Self Compacting Concrete – Determination of Confined Flowability in U – Shape Box, Italian Standards, 2003.
41. EN, B. 12390-3. Testing hardened concrete;part 3: compressive strength of test specimens. British Standards Institution. 2002.
42. ASTM C496/C496 M-11, Standard Test Method for Splitting Tensile Strength of Cylindrical Concrete Specimens, ASTM International, West Conshohocken, PA, 2011.
43. Amin A, Foster SJ, Muttoni A. Evaluation of the Tensile Strength of SFRC as derived from Inverse Analysis, VIII International Conference on Fracture Mechanics of Concrete and Concrete Structures, FraMCoS-8, p.9, Toledo, Spain, 2013.
44. Barros JA, Cunha VM, Ribeiro AF, Antunes JAB. Post-cracking behaviour of steel fibre reinforced concrete. Materials and Structures. 2005;38(1):47–56.
45. Jones PA, Austin SA, Robins PJ. Predicting the flexural load–deflection response of steel fibre reinforced concrete from strain, crack-width, fibre pull-out and distribution data. Materials and Structures. 2008;41(3):449–463.
46. Lee MK, Barr BIG. A four-exponential model to describe the behaviour of fibre reinforced concrete. Materials and structures. 2004;37(7):464–471.
47. Olesen JF. Fictitious crack propagation in fiber-reinforced concrete beams. Journal of Engineering Mechanics. 2001;127(3):272–280.
48. Ulfkjær JP, Krenk S, Brincker R. Analytical model for fictitious crack propagation in concrete beams. Journal of Engineering Mechanics. 1995;121(1):7–15.
49. Stephen SJ, Raphael B, Gettu R, Jose S. Determination of the tensile constitutive relations of fiber reinforced concrete using inverse analysis. Construction and Building Materials. 2019;195:405–414.
50. Jo BW, Shon YH, Kim YJ. The evaluation of elastic modulus for steel fiber reinforced concrete. Russian journal of nondestructive testing. 2001;37(2):152–161.
51. Gul M, Bashir A, Naqash JA. Study of modulus of elasticity of steel fiber reinforced concrete. International Journal of Engineering and Advanced Technology. 2014;3(4):304–309.